Effect of Mo:W ratio on segregation behavior and creep strength of nickel-based single crystal superalloys

Longfei Zhang[a], Zaiwang Huang[a], Liang Jiang[a], Junhua Luan[b], Zengbao Jiao[c], Chain Tsuan Liu[b]

[a]State Key Laboratory of Powder Metallurgy, Light Alloy Research Institute, Central South University, Changsha, Hunan, 410083, China
[b]Center for Advanced Structural Materials, Department of Materials Science and Engineering, City University of Hong Kong, Hong Kong, China
[c]Department of Mechanical Engineering, The Hong Kong Polytechnic University, Hong Kong, China

Abstract

In past decades, molybdenum (Mo) has demonstrated the potential to replace tungsten (W) in designing lighter nickel-based single crystal superalloys with enhanced creep resistance. In this research, three groups of nickel-based single crystal superalloys are designed and prepared by tuning the Mo:W ratio. The experimental observations show that the primary and secondary dendrite arm spacings are both independent on Mo:W ratio, but the γ/γ' eutectic volume fraction decreases as Mo:W ratio increases. The electron probe microanalysis reveals that Re, W and Co segregate to dendrite core regions, while Al, Ti, Cr, Mo and Ta to interdendritic regions. The microsegregation of Ta, W and Re are gradually relieved with increasing Mo:W ratio. Atom probe tomography results further indicate that Cr and Mo are depleted in γ/γ' eutectics, leading to the enrichment of Cr and Mo at interdendritic regions away from γ/γ' eutectics. Creep rupture results show that the rupture life at 1040 °C/145 MPa is improved as Mo:W ratio increases.

1. Introduction

Nickel-based single crystal superalloys are widely used for high-pressure turbine blades in industrial gas turbines and aero-engines [1]. These materials suffer temperatures up to about 1100 °C and high centrifugal stress due to their self-weights and high speed rotation in service. Therefore, improving mechanical properties at high temperatures, especially creep resistance, is pressingly desired. In past four decades, the chemistries of single crystal superalloys have been continuously refined. The major improvement in mechanical properties can be attributed to the increased levels of refractory metals. For example, the overall content of Mo, W, Re and Ta are 14 wt%, 17 wt% and 20 wt% in first-, second- and third-generation single crystal superalloys, respectively [1]. Unfortunately, increasing the amount of refractory elements deteriorates microsegregation inevitably.

In general, elemental microsegregation occurs during directionally solidified nickel-based superalloys spanning from dendrite core to interdendritic regions [2]. Previous literatures [3], [4], [5] have shown that alloying elements such as Co, W and Re prefer to segregate into the primary dendrite core regions while Al, Ti and Ta to the inter-dendritic regions, resulting in coarse γ′ precipitates and γ/γ′ eutectic pools formed in the latter regions. Severe microsegregation leads to the increased difficulty in subsequent solution heat treatment process [6], [7], [8], and the presence of γ/γ′ eutectics impairs the tensile and creep strength of superalloys [9]. Moreover, excessive local enrichment of solute atoms, such as Cr, Mo, W and Re, makes the alloys prone to the formation of brittle topological close-packed (TCP) phases [10], [11], resulting in degradation in mechanical properties [12]. Therefore, how to regulate element microsegregation remains to be an important aspect for alloy composition design.

Recently, developing low-rhenium (Re) and Re-free nickel-based superalloys becomes a hot topic with aims to lower cost and improve phase stability [13], [14], [15], [16]. To achieve this goal, W and Mo as two other potent solid solution strengtheners are supposed to increasingly add to improve creep strength. However, they have different effects on microsegregation and creep strength. It has been found that W tends to strongly segregate to dendrite core regions [3], [4], [5], [17], [18], [19], whereas whether Mo segregates to dendrite core [3], [4], [5] or interdendritic regions [19], [20], [21] remains hotly debated. Among these research, it is indicated that increasing Mo content can reduce the degree of microsegregation of Re and W [4], [20], [21]. In addition, although Mo is slightly weaker than W as a solid solution strengthener in γ matrix [22], it has a density nearly half of W, which indicates using Mo instead may improve the specific creep strength at high temperatures by reducing the alloy density. Therefore, it is of great interest to tune the Mo:W ratio to control the microsegregation and optimize the alloy density and creep resistance. In this research, three alloys with different Mo:W ratios are designed to address on this issue. The reverse segregation behavior of Mo is also explained using electron probe microanalysis (EPMA) and atom probetomography (APT). The effect of Mo:W ratio on segregation behavior and creep rupture life are comparatively investigated.

2. Materials and experimental

2.1. Alloy design

The second-generation single crystal superalloy CMSX-4 was chosen as the reference alloy. In newly-designed three alloys, in order to lower the cost, Re content was reduced to be half of that in CMSX-4, i.e., 0.5 at%. Meanwhile, the content of Mo + W was

increased from 2.5 at% to 3.1 at%. In addition, Ta content was increased from 2.2 at% to 2.5 at% in order to improve high temperature strength. Finally, Al, Cr, Co and Ti contents were balanced to obtain 60–70 vol% γ′ phase and adequate phase stability. Table 1 shows the nominal compositions of three alloys, with CMSX-4 included for comparison.

2.2. Experimental

The ingots of the alloys, with 60–80 mm in diameter and > 140 mm in length, were prepared by vacuum induction melting (VIM) and the compositions were measured by inductively-coupled plasma-optical emission spectroscopy (ICP-OES) at NCS Testing Technology Co., Ltd, China. Single crystal rods, with 15 mm in diameter and 170 mm in length, were directionally solidified using a conventional Bridgman method in a high rate solidification furnace (ALD furnace). The melting temperature was 1500 °C and the withdrawal rate of the mold was 3.0 mm/min. Cylindrical samples of 6 mm in diameter, 9 mm in length were machined for differential thermal analysis (DTA), which was performed on a EUROCAL EC2000 differential scanning calorimeter using a single-pan scanning technique [23], [24]. The DTA samples were heated up to 1420 °C at a rate of 10 °C/min and then cooled down at the same rate, protected by flowing pure argon at a rate of 40 ml/min. Thermodynamic calculations were also performed to obtain the phase transformation temperatures, using Thermo-Calc [25] with the TTNi8 database (ThermoTech Ltd., Guildford, United Kingdom). The alloy density was determined by a densimeter using Archimedes' principle.

The deviation angle between [001] crystallographic orientation and the axis of each rod was measured with the aid of Laue back scatter technique, and only those with the angles less than 7° were selected for the subsequent experiments. As directional

solidification proceeds in the furnace, the thermal gradient across solid-liquid interface typically decreases, resulting in gradient microstructure along the height of single crystal rods. To counteract this effect, (001) cross-sections at 5 mm above the bottom of single crystal rods, and (100) longitudinal-sections ranging from 5 mm to 15 mm away from the bottom were prepared using an electric spark cutter for each alloy. The sections were grinded, polished and etched with a solution of 33% HNO3, 33% acetic acid, 33% H2O, and 1% HF. The dendritic microstructures were then observed by an optical microscope (OM, Leica DM4000M) and a scanning electron microscope (SEM, FEI Quanta 650). Primary dendrite arm spacing (PDAS) was measured at the cross-section of each alloy, and calculated using an equation $\lambda 1 = (A/N)0.5$, where A was the area of the cross-section observed and N was the number of primary dendrites contained [26]. More than 900 primary dendrites were included to measure the average value for each alloy. Secondary dendrite arm spacing (SDAS) was measured on the longitudinal section by averaging the distance between 5 adjacent side branches of a primary dendrite [26]. More than 50 primary dendrites were included to obtain the average size of SDAS for each alloy. Quantitative analysis for volume fractions of γ/γ′ eutectics were performed on the cross-sections, using a method adapted from quantitative analysis of volume fraction of γ′ precipitates [27]. The average volume fraction of γ/γ′ eutectics was statistically measured on the cross-section from 15 different view-fields containing more than 30 primary dendrites.

Microprobe analysis was carried out on the polished cross-sections using a JXA-8530F electron probe microanalyzer (EPMA) equipped with 4 wavelength dispersive spectrometers (WDS). The WDS were configured with multiple crystal databases such as TAP (for Al, W and Ta), PETJ (for Ti, Mo and Re) and LIFH (for Ni, Co and W). Quantitative mapping was performed on an area with 200 points by 150 points at a step

size of 4 µm. The dwell time at each point was 30 ms. More than 30 quantitative point scans were performed for each alloy, with 10 at the dendrite core regions, 10 at the interdendritic regions away from γ/γ′ eutectics and 10 at the γ/γ′ eutectics. The acceleration voltage, probe current and probe diameter for the point analysis were 15 kV, 20 nA and 5 µm, respectively. X-ray counts were converted to chemical concentrations using the ZAF correction procedure.

The highest W content alloy, 1.0Mo2.1W, was examined by atom probe tomography (APT) to measure the elemental partitioning between γ and γ′ phases. Needle-shaped specimens required for APT were fabricated by lift-outs and annular milled in a FEI Scios focused ion beam/scanning electron microscope (FIB/SEM). The APT characterizations were performed in a local electrode atom probe (CAMEACA LEAP 5000 XR). The specimens were analyzed at 50 K in voltage mode with a pulse repetition rate of 200 kHz, a pulse fraction of 20%, and an evaporation detection rate of 0.5% atom per pulse. Imago Visualization and Analysis Software (IVAS) version 3.8 was used for creating the 3D reconstructions and data analysis.

The single crystal rods of three alloys were finally subjected to a solution heat treatment at 1310 °C/12 h then air quenched, followed by two stages of ageing treatment at 1080 °C/4 h and 870 °C/16 h. The γ and γ′ phase lattice parameters were calculated with JMatPro software [28]. Specimens of 25 mm gauge length and 5 mm diameter were machined from the heat treated rods. Creep rupture tests were performed at 850 °C/650 MPa, 982 °C/248 MPa and 1040 °C/145 MPa by RD2-3 type creep testing machine. Metallographic samples from heat treated rods and ruptured specimens were prepared and etched by the same methods as mentioned above, then examined by SEM observation.

3. Results and discussion

3.1. Microstructure and thermodynamics

Table 2 shows the alloy compositions determined by ICP-OES, also included are the alloy densities. The actual compositions of the alloys were in excellent agreement with the nominal compositions shown in Table 1. The alloy density was decreased by nearly 2% as Mo:W ratio increased from 1.0:2.1–2.5:0.6.

The optical micrographs of microstructure in as-cast alloy 1.0Mo2.1W are shown in Fig. 1. From cross section, the dendrite arms appeared in cross-like morphology, with γ/γ' eutectic pools situated inside the interdendritic regions, as shown in Fig. 1a. From longitudinal section, the primary dendrite arms were parallel to the [001] growth direction, whereas the secondary dendrite arms were perpendicular to and uniformly distributed along the primary dendrites, as shown in Fig. 1b. Similar dendritic morphology was observed for alloy 1.75Mo1.35W and 2.5Mo0.6W.

Secondary electron micrographs on the cross-section of as-cast alloy 1.0Mo2.1W are shown in Fig. 3. Comparing with the dendritic morphology as shown in Fig. 1a, three different regions could be discriminated: (1) fine and cuboidal γ' precipitates embedded within γ matrix at dendrite core (DC) regions, as shown in Fig. 3b, (2) coarser and irregularly-shaped γ' precipitates in interdendritic (ID) regions, as shown in Fig. 3c, and (3) γ/γ' eutectic pools with about 50 µm in size inside ID regions, as shown in Fig. 3d. No other phases, such as Mo-rich phases [20] or α-(W, Mo) phases [29], were observed. This could be attributed to relatively low overall content of Mo and W in these alloys.

Fig. 4 shows the heating curves of three alloys from DTA. The liquidus (TL) and the solidus (TS) temperatures were determined by the peak and the onset temperatures of the endothermic peak, respectively [30]. Table 3 lists the thermodynamic data both extracted from the heating curves and calculated with Thermo-Calc. As shown in Table 3, the DTA results and the thermodynamic calculation indicated that both the liquidus and solidus temperatures were decreased as Mo:W ratio increased, however, the solidification intervals, i.e. TL-TS, remained nearly unaltered. Similar thermodynamic trends with Mo and W were also observed by C. Ai et al. [20].

Based on the thermodynamic results, the independence of PDAS ($\lambda 1$) and SDAS ($\lambda 2$) on Mo:W ratio can be rationalized as follows. Similar to binary alloys, either $\lambda 1$ or $\lambda 2$ in directionally solidified superalloys are functions of temperature gradient (G) and growth rate (R), described as [26], [31], [32], [33], [34]:(1)(2)where $\mu 1$, $\mu 2$, and exponents a, b and c are all constants for a given composition. First of all, either $\mu 1$ or $\mu 2$ are considered as identical for these three alloys, since their compositions are similar even though a slight variation of Mo:W ratio. This simplification can be further justified with three parameters primarily affecting $\mu 1$ and $\mu 2$, including Gibbs-Thomson coefficient, solute diffusivity in the liquid and the solidification interval [17], [35]. (1) It is indicated that Gibbs-Thomson coefficient is independent on the liquid composition in binary alloys [36], therefore the variation of Mo:W ratio may not change the Gibbs-Thomson coefficient significantly. (2) It has been measured that Mo and W have quite similar solute diffusivities in liquid nickel [37], and (3) the liquidus-solidus intervals are independent of the Mo:W ratio, as indicated in Table 3. Secondly, the constants a and b for $\lambda 1$ are about 1/2 and 1/4, respectively, and the constant c for $\lambda 2$ is about 1/3 in directionally solidified superalloys [17], [26], [38]. At last, since the

samples came from the same height of single crystal rods, both temperature gradient G and growth rate R were assumed as constants for three alloys. Therefore, it is reasonable to see that PDAS and SDAS remain unchanged as Mo:W ratio increases. The effect of Mo:W ratio on the volume fraction of γ/γ′ eutectics can be considered from the non-equilibrium solidification process. Fig. 5 shows the solidification sequence of the three alloys calculated by Scheil model with Thermo-Calc. It is indicated that, as the Mo:W ratio increases, the fraction of primary γ phase increases during solidification, leading to the deceases of γ/γ′ eutectic fraction.

3.2. Segregation behavior of alloying elements

The EPMA mapping scan for all the alloying elements in as-cast alloy 1.0Mo2.1W are shown in Fig. 7. Comparing with the microstructure in Fig. 3, the mapping scan clearly indicated that element Al, Ti and Ta segregated to ID regions and reached highest concentrations at γ/γ′ eutectic pools, as shown in Fig. 7a, b and c, on the contrary, element Co, W and Re were depleted in γ/γ′ eutectic pools and segregated to DC regions, as shown in Fig. 7d, e and f. Although elements Cr and Mo segregated to ID regions, they were depleted in γ/γ′ eutectic pools, as shown in Fig. 7g and h. Similar microsegregation trends were also observed in as-cast alloy 1.75Mo1.35W and 2.5Mo0.6W.

The average composition of quantitative point scans at DC, ID regions and γ/γ′ eutectics for three alloys are listed in Table 4, wherein the ID regions refer to the regions consisting of coarser γ′ precipitates but away from the γ/γ′ eutectics as shown in Fig. 3. The degree of microsegregation of elements between the DC and ID regions can be characterized by the segregation partitioning term, $k' = C_{DC}/C_{ID}$,

where C_{DC} and C_{ID} are the concentrations of an element at DC and ID regions, respectively. $k' > 1$ means this element segregates to DC regions, and $k' < 1$ means the element segregates to ID regions. Similarly, to determine the element microsegregation degree between DC regions and γ/γ′ eutectics, another segregation partitioning term k'' can be expressed as $k'' = C_{DC}/C_E$, where C_E is the concentration of an element at γ/γ′ eutectics. The average segregation partitioning coefficients for the three alloys are also listed in Table 4. From EPMA results in Table 4, it indicated that the compositions of Ta, Al and Ti, which were γ′ forming elements, tended to increase at DC but decrease at both ID regions and γ/γ′ eutectics as Mo:W ratio increased. This could also explain the reduction of γ/γ′ eutectic fraction with Mo:W ratio as shown in Fig. 2.

Based on Ni-X binary phase diagrams, the segregation of an alloying element X should obey the following rule: the element that increases the solidus temperature segregates to DC regions, otherwise it segregates to ID regions. Both the partitioning coefficients k' and k'' demonstrated that Co, W and Re segregated to DC regions and Al, Ti and Ta to ID regions, as shown in Table 4, which obeyed the above rule and were consistent with previous studies [3], [4], [5]. For the microsegregation behavior of Cr and Mo, although they reduced the solidus temperature [39], [40], they were identified to segregate to DC regions in some superalloys [3], [18], [21]. According to the results in Table 4, it was clear that when k' was employed to evaluate the segregation direction, Cr and Mo segregated to ID regions, except for Cr in alloy 1.0Mo2.1W. However, the segregation coefficient k'' reversely indicated that Cr and Mo segregated to DC regions. Comparing to the characterization methods used in literature [3], [18], [21], it was known that using k'' would result in the observation that Cr and Mo segregate to DC regions.

Since the γ/γ′ eutectics are primarily composed of coarse γ′ phases, as shown in Fig. 3d, the elemental solubility in γ′ phase has to be related to the microsegregation behavior. Fig. 8 shows the 3D atom probe reconstructions and elemental distributions between the γ and γ′ phases for alloy 1.0Mo2.1W. Combining the EPMA results in Fig. 7 and Table 4, it showed that Al, Ti and Ta segregating to ID regions strongly partitioned to γ′ phase, whereas Co and Re segregating to DC regions strongly partitioned to γ phase. Although W segregated to DC regions, it was almost evenly distributed between γ and γ′ phase. However, Cr and Mo segregating in ID regions strongly depleted in γ′ phase. From this low solubility of Cr and Mo in γ′ phase, it can be speculated that, at the last stage of solidification, although Cr and Mo segregate to ID regions, they are rejected from primary γ′ phases in γ/γ′ eutectics, resulting in the enrichment of Cr and Mo at the ID regions away from the γ/γ′ eutectics.

Since γ/γ′ eutectics were depleted in Cr and Mo, their compositions were not representative of that of the melt in ID regions during solidification. Moreover, since very small volume fractions of γ/γ′ eutectics were observed in the experimental alloys, it was more rational to employ the compositions at ID regions away from the γ/γ′ eutectics to characterize the microsegregation degree. Fig. 9 depicts the dependence of segregation coefficients k' for element Ta, Cr, Mo, W and Re on Mo:W ratio. It was evident that, as the Mo:W ratio increased, the W and Re segregation coefficients decreased significantly and Cr and Mo tended to slightly decrease, while Ta slightly increased, leading to the lowest microsegregation degree for refractory elements in alloy 2.5Mo0.6W.

It was worth noting in ref. [18] that, although Mo was identified to segregate to the DC, the EPMA line-scan results indicated an enrichment of Mo at the ID regions away from

γ/γ′ eutectics. Moreover, many other studies also show that the microsegregation of Cr and/or Mo behave in the same manner [17], [20], [41], [42]. Therefore, the distribution pattern for alloying elements in as-cast single crystal superalloys can be summarized in Fig. 10, where the special pattern for Cr and Mo enriched in ID regions but depleted in γ/γ′ eutectics is addressed, resulting in the reverse segregation direction between k' and k'' for Cr and Mo.

The influence of Mo:W ratio on microsegregation behavior can be explained with the Ni-Mo [40] and Ni-W [43] binary phase diagrams. At the Ni-rich end of the phase diagrams, one can see that as the concentration of alloying element increases, the concentration gap between solidus and liquidus increases at freezing temperature. Therefore, the degree of microsegregation increases with the solute concentration. As Mo was increased at the expense of W here, it was reasonable to see the degree of W microsegregation decreased while that of Mo increased with Mo:W ratio.

The reduction of Re microsegregation degree with Mo and W was consistent with previous researches [20], [21]. R.A. Hobbs et al. [21] argued that a strong interplay might exist between Cr, Mo, W and Re, as Cr-Re, Mo-Re and W-Re tended to combine to form stable TCP phases. C. Ai et al. [20] considered the strong binding forces between W-Re and Mo-Re atoms, and argued that substituting Mo for W could relieve the Re microsegregation because W and Mo prefer to segregate to DC and ID regions, respectively. As indicated in Fig. 8, it was interesting to see that, as the Mo:W ratio increased, Cr, Mo, W and Re exhibited the same microsegregation change direction toward ID regions. This phenomenon also demonstrates that strong interactions exist among these four elements for TCP phases formation.

The reduction of Ta microsegregation degree was out of expectation since no significant relief to Ta segregation has been observed upon addition of Mo [20], [21]. This might be attributed to the characterization method, in which the compositions of γ/γ′ eutectics which significantly enriched in Ta were not taken into considerations. However, since the γ/γ′ eutectic volume fraction reduced as Mo:W ratio increased, as shown in Fig. 2, this could also demonstrate that Ta microsegregation was relieved by increasing Mo:W ratio.

3.3. Creep rupture

The creep rupture results of heat treated alloys are given in Fig. 11a, and the Larson-Miller diagrams are shown in Fig. 11b, with the nominal diagrams of CMSX-4 and René N5 included for reference, which are taken from the literature [44].

At 850 °C/650 MPa, the creep rupture lives of three alloys were nearly identical, which indicated that the creep rupture life was almost independent of Mo:W ratio at this condition. As the Mo:W ratio increased, the rupture life at 982 °C/248 MPa reduced slightly, and it was interesting to see that the life at 1040 °C/145 MPa was improved, as shown in Fig. 11a. The creep performance of three alloys were found to be comparable to CMSX-4 and René N5 at three test conditions, as shown in Fig. 11b, although they only had half of the Re content.

Fig. 12 depicts the microstructure near fractured surface of alloy 2.5Mo0.6W at different test conditions. As shown in Fig. 12, micro-pores generally lay in the center of the micro-cracks, which propagated perpendicularly to the direction of applied stress. The micro-pores were stretched along the applied stress, indicating significant creep deformation had occurred. After fracture, the γ′ precipitates remained cuboidal shape at 850 °C/650 MPa, as shown in Fig. 12a, which are similar to the original morphology.

However, γ′ precipitates coalesced into rafts at 982 °C/248 MPa, as shown in Fig. 12b. γ′ rafts also formed at 1040 °C/145 MPa after fracture but were thicker and less continuous as shown in Fig. 12c. No TCP phases were observed at present experimental conditions. Similar microstructures were also observed in alloy 1.0Mo2.1W and 1.75Mo1.35W after creep ruptures.

It is known that creep deformation mechanisms of single crystal superalloys can be divided into three regimes, i.e. primary creep, tertiary creep and rafting regimes [45]. Creep at 850 °C/650 MPa typically falls into the primary creep regime, where γ′ coarsening is absent, as shown in Fig. 12a, and significant primary creep deformation occurs by shearing the γ′ precipitates. Therefore, precipitation hardening is the main factor for strengthening. The independence of creep rupture life on Mo:W ratio at this condition might be ascribed to nearly identical γ′ fractions in three alloys. However, γ′ rafting occurs significantly at 1040 °C/145 MPa as shown in Fig. 12c, indicating that creep deformation goes into the rafting regimes. In this regime, creep dislocationsinitiate in γ matrix and get deposited at γ/γ′ interfaces by thermal activation, forming equilibrium dislocation networks at the interfaces and thus relieving the interfacial mismatch, followed by formation of γ′ rafts. The steady creep rate is found to reduce with the decrease of dislocation spacing in the network, which is related to the γ/γ′ lattice mismatch [46], [47]. The γ/γ′ mismatches of three alloys at 1040 °C are calculated with JMatPro software and the results are shown in Table 5. It indicates that the γ/γ′ mismatch becomes more negative with the increase of Mo:W ratio, which is in favor of forming more dense dislocation network, resulting in the improvement in creep life.

Another important factor for creep strength at high temperature is the solid solution strengthening of γ matrix. This can be evaluated with the concentrations of Re, W and Mo in the γ matrix, which are the most effective solid solution strengtheners in superalloys. It is experimentally determined that Re is about twice as effective (in at%) compared to W and 2.4 times as effective as Mo in γ matrix [22]. Table 5 also shows the element partitioning coefficients $k = xi\gamma/xi\gamma'$ calculated at 1040 °C with Thermo-Calc, with $xi\gamma$ and $xi\gamma'$ being the atomic fractions of element i in γ and γ′ phases, respectively. It is indicated that Re and Mo strongly partition to γ matrix but W distributes more evenly between γ and γ′ phases, which is consistent with the APT results as shown in Fig. 8. As the Mo:W ratio increases, although the partitioning degree of W and Mo are slightly reduced, that of Re is promoted more profoundly. This means that Re can be utilized more efficient in strengthening γ phase by increasing the Mo:W ratio, also leading to the improvement in creep life.

The creep property at 982 °C/248 MPa remained in controversy with the discussion above. Although it seemed in the raft regime as well, as shown in Fig. 12b, the creep life decreased with Mo:W ratio. However, creep deformation at this intermediate condition is supposed to in the tertiary creep regime [45]. To understand this behavior, further investigation needs to be carried out on the creep mechanism at this condition.

4. Conclusions

Through designing and investigating three nickel base single crystal superalloys with different Mo:W ratios, the following conclusions were made:

(1) The primary dendrite arm spacing and secondary dendrite arm spacing were observed to be independent of the Mo:W ratio, while the volume fraction of γ/γ′ eutectics decreased by increasing the Mo:W ratio.

(2) Alloying elements Cr and Mo tended to segregate to interdendritic regions, but their depletions in the interdendritic γ/γ′ eutectics result in the enrichment of Cr and Mo at the interdendritic regions away from γ/γ′ eutectics. As Mo:W ratio increased, the microsegregation degree of Re and W to dendrite core and Ta to interdendritic regions were reduced, but Mo to interdendritic regions was increased.

(3) Creep rupture life at 1040 °C/145 MPa was improved by increasing the Mo:W ratio.

Acknowledgement

Data availability

The raw data and processed data required to reproduce these findings cannot be shared at this time as the data also forms part of an ongoing study.

References

[1] P. Caron, T. Khan, Evolution of Ni-based superalloys for single crystal gas turbine blade applications, Aerosp. Sci. Technol. 3 (1999) 513–523.

[2] M.Durand-Charee,TheMicrostructureofSuperalloys,CRCPress,LLC,BocaRaton, 1997, p. 60.

[3] A.I. Epishin, I.L. Svetlov, N.V. Petrushin, Y.V. Loshchinin, T. Link, Segregation in

single-crystal nickel-base superalloys, Defect Diffus. Forum 309- 310 (2011) 121–126.

[4] E.C. Caldwell, F.J. Fela, G.E. Fuchs, The segregation of elements in high-refractory-content single-crystal nickel-based superalloys, JOM 56 (2004) 44–48.

[5] S. Tin, T.M. Pollock, Phase instabilities and carbon additions in single-crystal nickel-base superalloys, Mater. Sci. Eng. A 348 (2003) 111–121.

[6] G.E.Fuchs,SolutionheattreatmentresponseofathirdgenerationsinglecrystalNi- base superalloy, Mater. Sci. Eng. A 300 (2001) 52–60.

[7] B.C. Wilson, J.A. Hickman, G.E. Fuchs, The effect of solution heat treatment on a single-crystal Ni-based superalloy, JOM 55 (2003) 35–40.

[8] F. Long, Y.S. Yoo, S.M. Seo, T. Jin, Z.Q. Hu, C.Y. Jo, Effect of Re addition and withdrawal rate on the solidification behavior of directionally solidified superalloy AM3, J. Mater. Sci. Technol. 27 (2011) 101–106.

[9] B.C. Yan, J. Zhang, L.H. Lou, Effect of boron additions on the microstructure and transverse properties of a directionally solidified superalloy, Mater. Sci. Eng. A 474 (2008) 39–47.

[10] M.S.A. Karunaratne, C.M.F. Rae, R.C. Reed, On the microstructural instability of an experimental nickel-based single-crystal superalloy, Metall. Mater. Trans. A Phys. Metall. Mater. Sci. 32 (2001) 2409–2421.

[11] C. Rae, Alloys by Design: modelling next generation superalloys, Mater. Sci. Technol. 25 (2009) 479–487.

[12] R.A. MacKay, T.P. Gabb, M.V. Nathal, Microstructure-sensitive creep models for nickel-base superalloy single crystals, Mater. Sci. Eng. A 582 (2013) 397–408.

[13] P.J. Fink, J.L. Miller, D.G. Konitzer, Rhenium reduction-alloy design using an economically strategic element, JOM 62 (2010) 55–57.

[14] J. Wahl, K. Harris, New single crystal superalloys - overview and update, MATEC

Web Conf. 14 (2014) 17002.

[15] R. Rettig, K. Matuszewski, A. Müller, H.E. Helmer, N.C. Ritter, R.F. Singer, Development of a low-density rhenium-free single crystal nickel-based superalloy by application of numerical multi-criteria optimization using thermodynamic calculations, Superalloys 2016 (2016) 35–44.

[16] J. Gong, D. Snyder, T. Kozmel, C. Kern, J.E. Saal, I. Berglund, J. Sebastian, G. Olson, ICME design of a castable, creep-resistant, single-crystal turbine alloy, JOM 69 (2017) 880–885.

[17] G. Matache, D.M. Stefanescu, C. Puscasu, E. Alexandrescu, Dendritic segregation and arm spacing in directionally solidified CMSX-4 superalloy, Int. J. Cast. Met. Res. 29 (2016) 303–316.

[18] R.M. Kearsey, J.C. Beddoes, K.M. Jaansalu, W.T. Thompson, P. Au, The Effects of Re, W and Ru on microsegregation behaviour in single crystal superalloy systems, Superalloys 2004 (2004) 801–810.

[19] S.M. Seo, J.H. Lee, Y.S. Yoo, C.Y. Jo, H. Miyahara, K. Ogi, A comparative study of the γ/γ′ eutectic evolution during the solidification of Ni-base superalloys, Metall. Mater. Trans. A Phys. Metall. Mater. Sci. 42 (2011) 3150–3159.

[20] C. Ai, L. Liu, J. Zhang, M. Guo, Z. Li, T. Huang, J. Zhou, S. Li, S. Gong, G. Liu, Influence of substituting Mo for W on solidification characteristics of Re-containing Ni based single crystal superalloy, J. Alloy. Compd. 754 (2018) 85–92.

[21] R.A. Hobbs, S. Tin, C.M.F. Rae, R.W. Broomfield, C.J. Humphreys, Solidification characteristics of advanced nickel-base single crystal superalloys, Superalloys 2004 (2004) 819–825.

[22] E. Fleischmann, M.K. Miller, E. Affeldt, U. Glatzel, Quantitative experimental determination of the solid solution hardening potential of rhenium, tungsten and

molybdenum in single-crystal nickel-based superalloys, Acta Mater. 87 (2015) 350–356.

[23] S. Savas, H. Dong, Determination of solid / liquid fraction of three aluminum binary alloys using a new single-pan scanning calorimeter, J. Therm. Anal. Calorim. 130 (2017) 1847–1854.

[24] H. Dong, J.D. Hunt, A comparison of a novel single-pan calorimeter with a conventional heat-flux differential scanning calorimeter, High Temp. - High Press. 32 (2000) 311–319.

[25] B. Sundman, B. Jansson, J.O. Andersson, The thermo-calc databank system, Calphad 9 (1985) 153–190.

[26] M. Vijayakumar, S.N. Tewari, J.E. Lee, P.A. Curreri, Dendrite spacings in directionally solidified superalloy PWA-1480, Mater. Sci. Eng. A 132 (1991) 195–201.

[27] P.M. Mignanelli, N.G. Jones, M.C. Hardy, H.J. Stone, The influence of Al: Nb ratio on the microstructure and mechanical response of quaternary Ni-Cr-Al-Nb alloys, Mater. Sci. Eng. A 612 (2014) 179–186.

[28] N. Saunders, U.K.Z. Guo, X. Li, A.P. Miodownik, J.-P. Schillé, Using JMatPro to model materials properties and behavior, JOM 55 (2003) 60–65.

[29] T. Zhou, W. Feng, H. Zhao, Y. Meng, H. Zhang, H. Ding, Z. Wang, Coupling effects of tungsten and molybdenum on microstructure and stress-rupture properties of a nickel-base cast superalloy, Prog. Nat. Sci. Mater. Int. 28 (2018) 45–53.

[30] W.J. Boettinger, U.R. Kattner, K.-W. Moon, J.H. Perepezko, DTA and heat-flux DSC measurements of alloy melting and freezing, 2007.

[31] H.A. Palacio, M. Solari, H. Biloni, Microsegregation in cellular dendritic growth in binary alloys of Al-Cu, J. Cryst. Growth 73 (1985) 369–378.

[32] S. Kostic, A. Golubovic, A. Valcic, Primary and secondary dendrite spacing of Ni-

based superalloy single crystals, J. Serb. Chem. Soc. 74 (2009) 61–69.

[33] K.P. Young, D.H. Kerkwood, The dendrite arm spacings of aluminum-copper alloys solidified under steady-state conditions, Metall. Trans. A 6 (1975) 197–205.

[34] D.G. McCartney, J.D. Hunt, Measurements of cell and primary dendrite arm spacings in directionally solidified aluminium alloys, Acta Metall. 29 (1981) 1851–1863.

[35] D.M. Stefanescu, Science and Engineering of Casting Solidification, 2nd ed., Springer, US, New York, 2009.

[36] U. Böyük, N. Maraşli, Investigation of liquid composition effect on Gibbs-Thomson coefficient and solid-liquid interfacial energy in SCN based binary alloys, Mater. Charact. 59 (2008) 998–1006.

[37] J.P. Leonard, T.J. Renk, M.O. Thompson, M.J. Aziz, Solute diffusion in liquid nickel measured by pulsed ion beam melting, Metall. Mater. Trans. A Phys. Metall. Mater. Sci. 35 A (2004) 2803–2807.

[38] L. Li, R.A. Overfelt, Influence of directional solidification variables on the cellular and primary dendrite arm spacings of PWA1484, J. Mater. Sci. 37 (2002) 3521–3532.

[39] D.S. Bloom, N.J. Grant, Chromium-nickel phase diagram, JOM 3 (1951) 1009.

[40] H. Okamoto, Mo-Ni (molybdenum-nickel), J. Phase Equilibria. 12 (1991) 703.

[41] V.A. Wills, D.G. McCartney, A comparative study of solidification features in nickel-base superalloys: microstructural evolution and microsegregation, Mater. Sci. Eng. A 145 (1991) 223–232.

[42] A. Heckl, R. Rettig, S. Cenanovic, M. Gken, R.F. Singer, Investigation of the final stages of solidification and eutectic phase formation in Re and Ru containing nickel-base superalloys, J. Cryst. Growth 312 (2010) 2137–2144.

[43] H. Okamoto, Ni-W (nickel-tungsten), J. Phase Equilibria. 12 (1991) 706.

[44] J.B. Wahl, K. Harris, New single crystal superalloys CMSX®-7 and CMSX®-8, Superalloys (2012) 179–188.

[45] R.C. Reed, The Superalloys: Fundamentals and Applications, Cambridge University

Press, Cambridge, 2006, p. p172.

[46] Y. Koizumi, T. Kobayashi, T. Yokokawa, J. Zhang, M. Osawa, H. Harada, Y. Aoki, M. Arai, Development of next-generation Ni-base single crystal super alloys, Superalloys (2004) 35–43.

[47] J.X. Zhang, J.C. Wang, H. Harada, Y. Koizumi, The effect of lattice misfit on the dislocation motion in superalloys during high-temperature low-stress creep, Acta Mater. 53 (2005) 4623–4633.
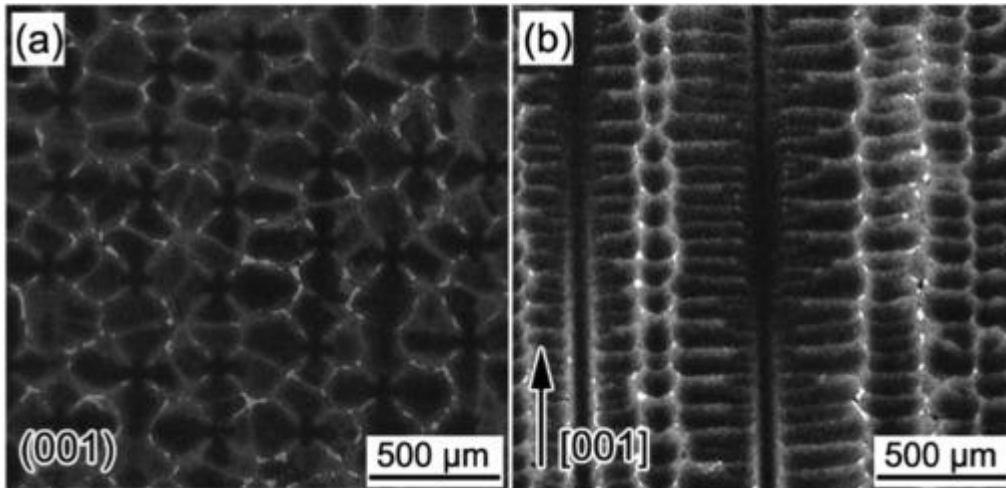
Fig. 1. Optical images of dendrite morphologies at (a) cross-sections and (b) longitudinal sections of alloy 1.0Mo2.1W.
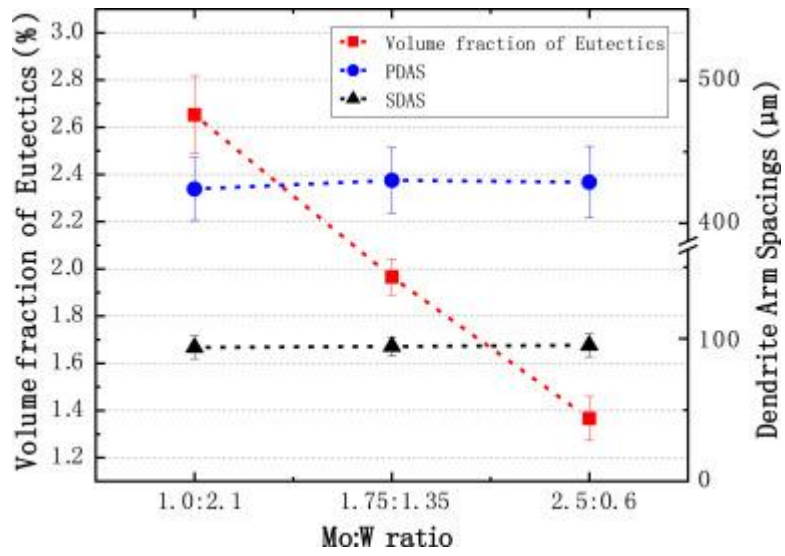
Fig. 2. Dependence of PDAS, SDAS and volume fraction of γ/γ′ eutectics on Mo:W

ratio.
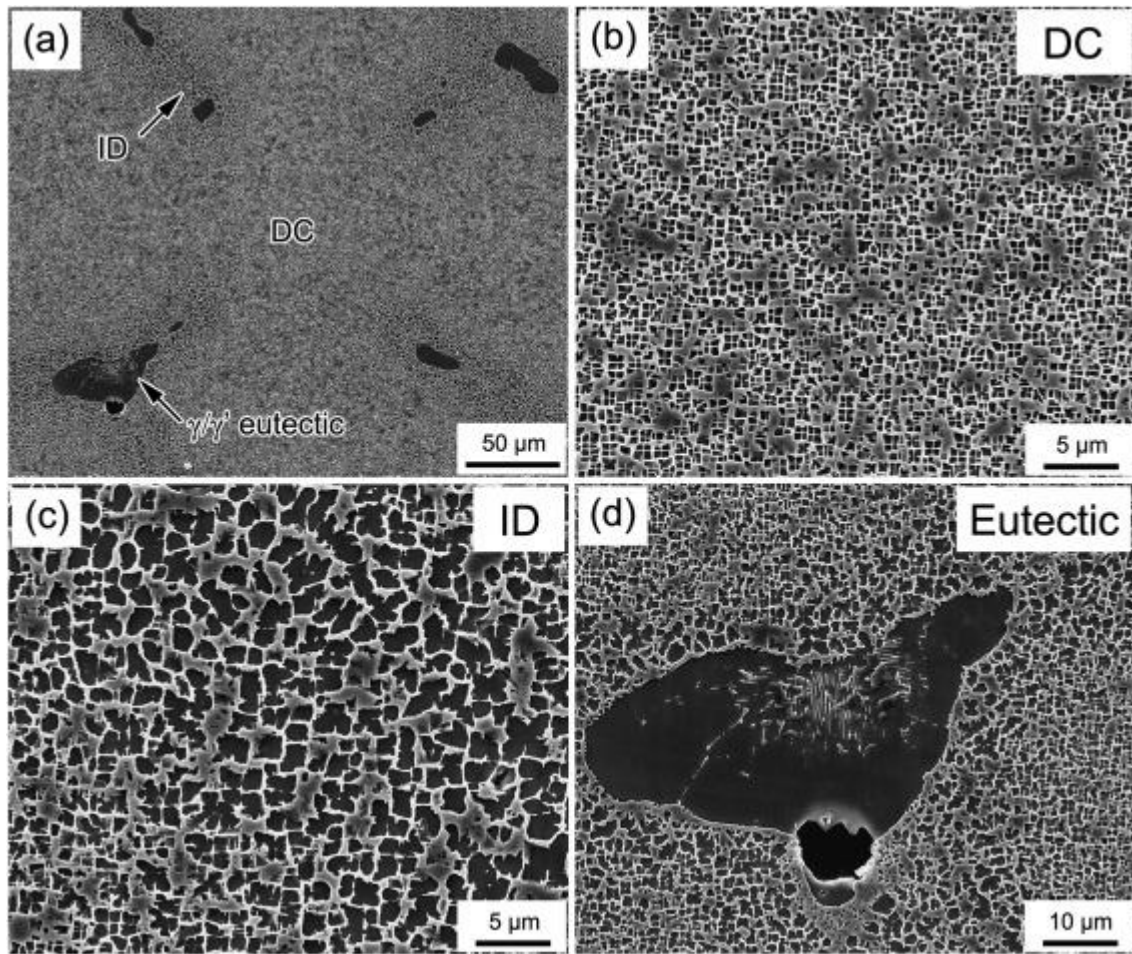
Fig. 3. Secondary electron micrographs of as-cast alloy 1.0Mo2.1W on the cross-section: (a) a full dendrite, (b) dendrite core (DC) regions consisting of fine γ′ precipitates, (c) interdendritic (ID) regions consisting of coarser γ′ precipitates, (d) γ/γ′ eutectic pool inside ID regions.
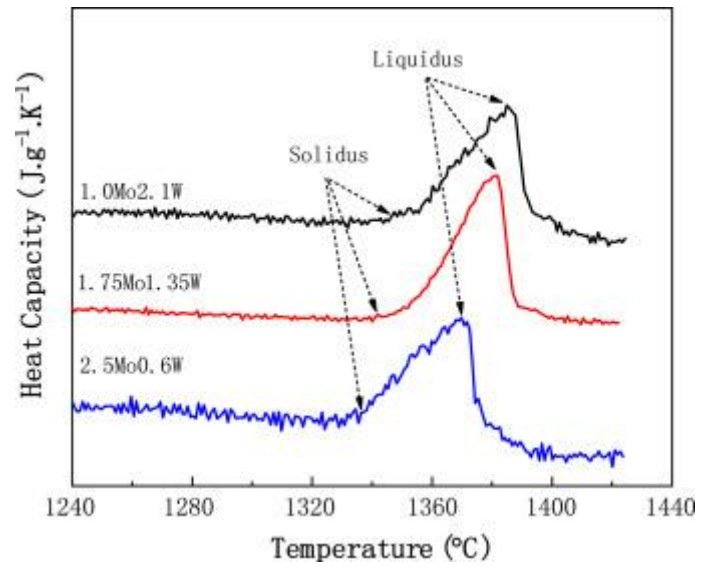
Fig. 4. The heating curves of three alloys from DTA tests.
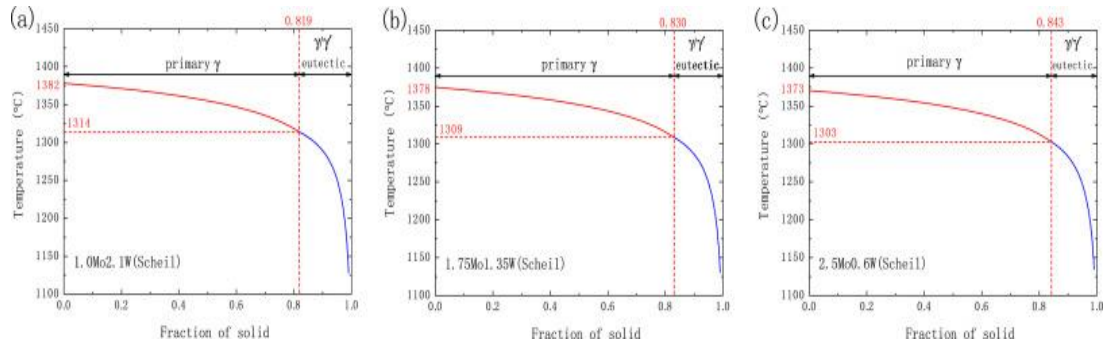
Fig. 5. Solidification sequence of three alloys calculated by Scheil model. (a)

1.0Mo2.1W, (b) 1.75Mo1.35W, (c) 2.5Mo0.6W.
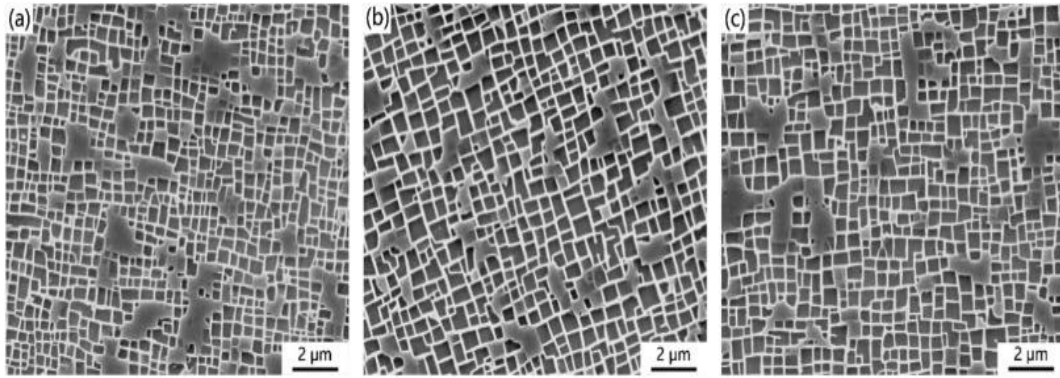
Fig. 6. The microstructure of heat treated alloys. (a) 1.0Mo2.1W, (b) 1.75Mo1.35W,

(c) 2.5Mo0.6W.
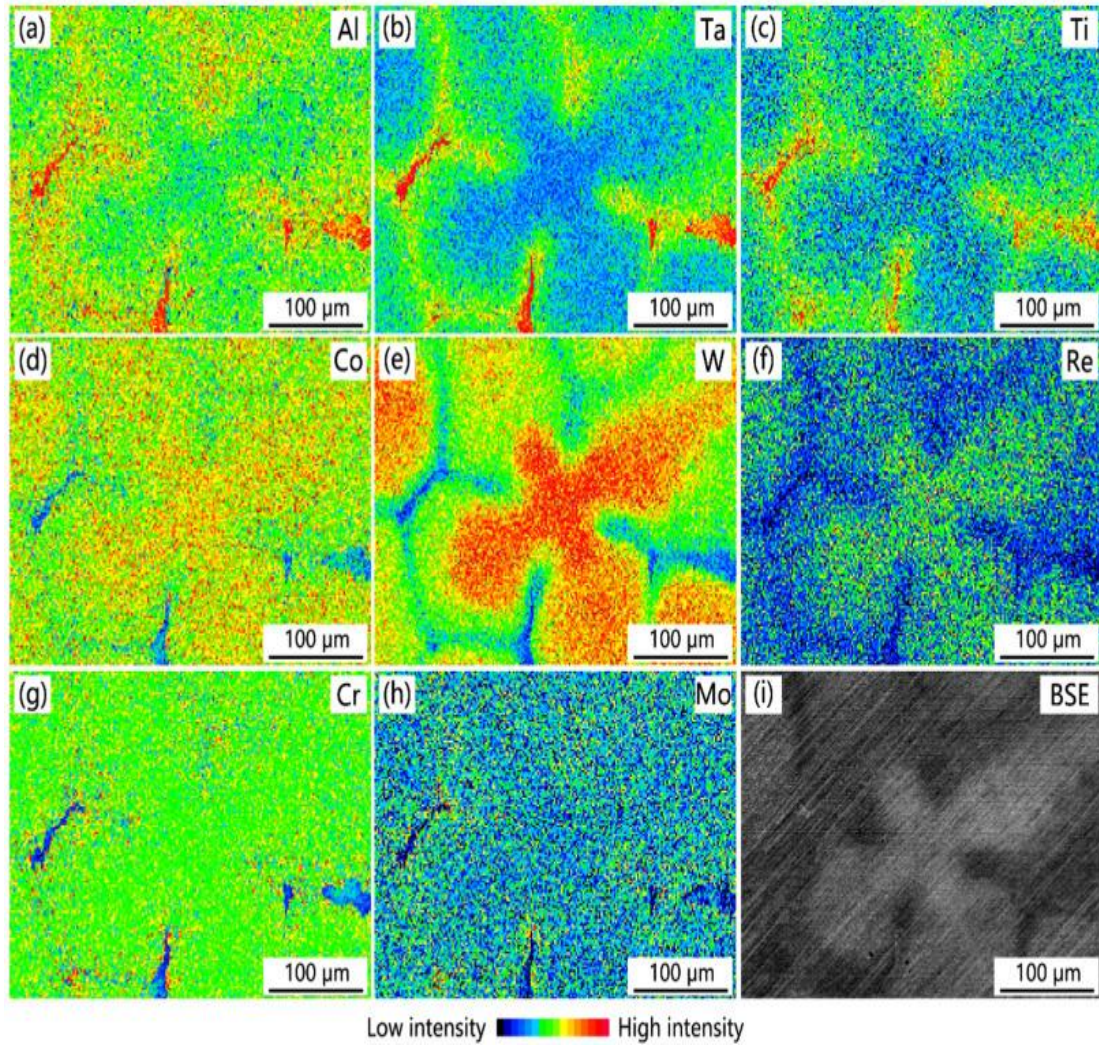
Fig. 7. EPMA mapping scan of alloy 1.0Mo2.1W. (a)-(h) distribution of each alloying element, (i) backscattered electron (BSE) image of the same area.
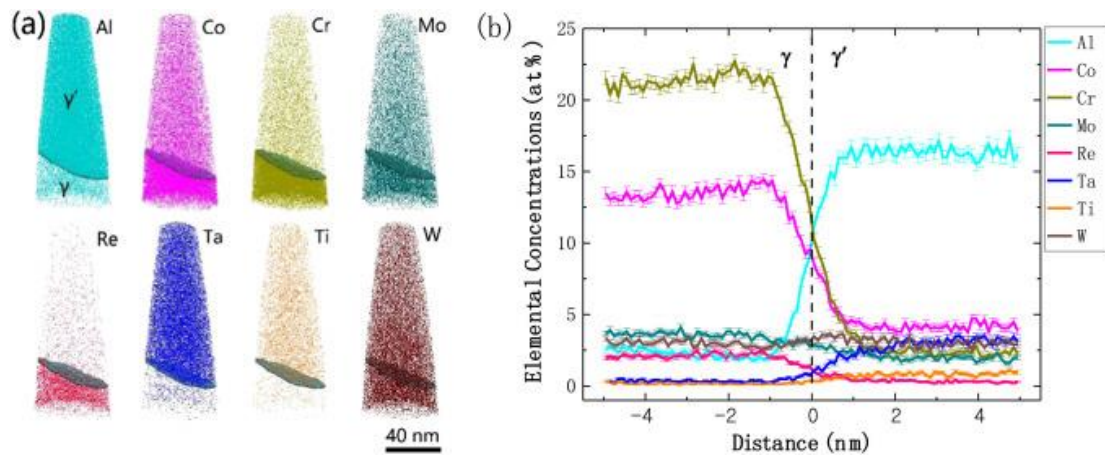
Fig. 8. (a) 3D atom probe reconstructions of spatial distributions of all alloying elements through the tip sample analyzed for alloy 1.0Mo2.1W. The interface between γ and γ′ phase is visualized by the 9.0 at% Al concentration isosurface. (b) Proximity histogram of elemental concentrations across the γ/γ′ interface.
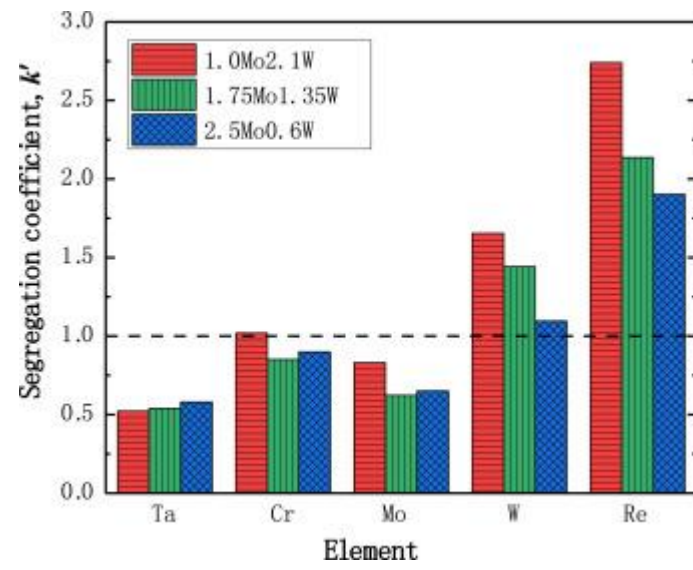
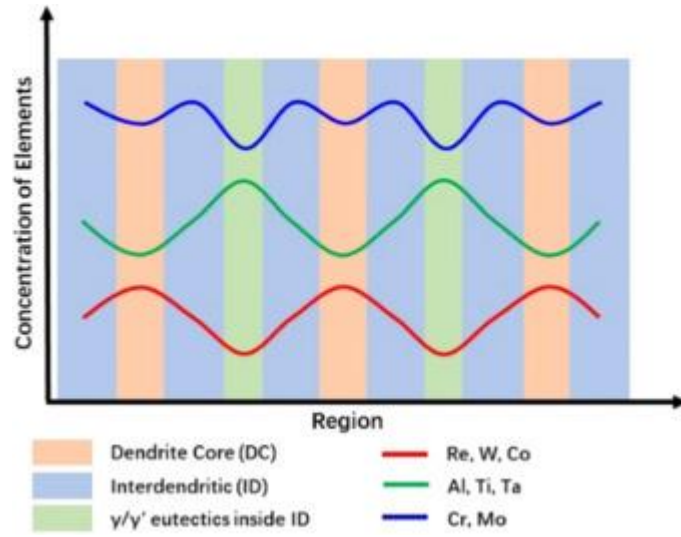Fig. 9. Change of segregation behavior for Ta, Cr, Mo, W and Rewith Mo:W ratio.

Fig. 10. Schematic of distribution pattern for alloying elements in as-cast single
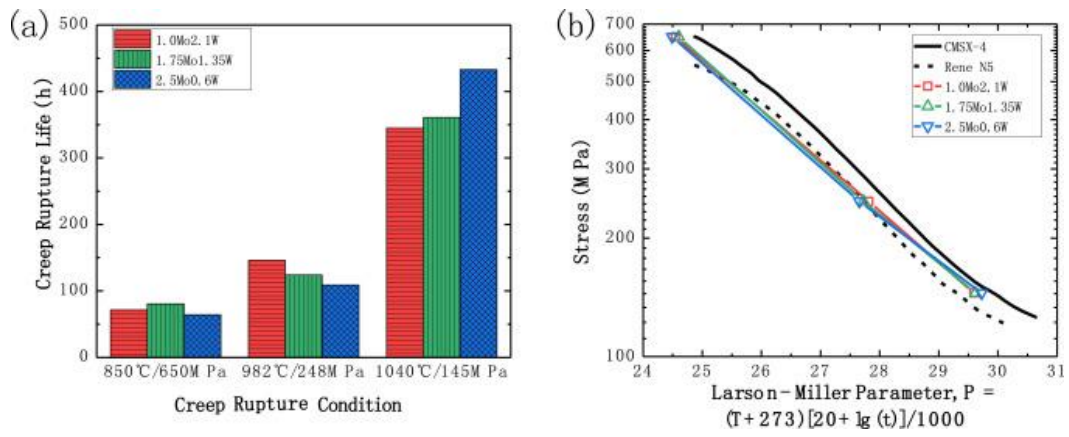
crystal superalloys.

Fig. 11. (a) Creep rupture life of three heat treated alloys at different test conditions and (b) Larson-Miller diagrams comparing to the alloys CMSX-4 and René N5.
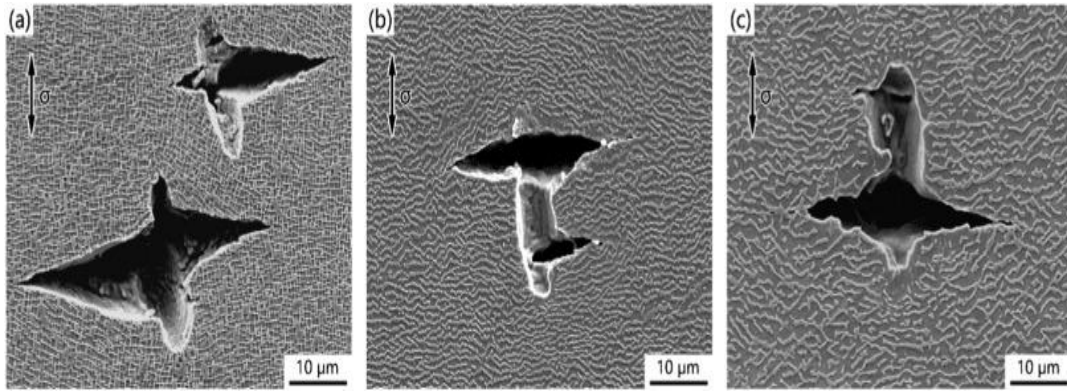
Fig. 12. The microstructure of creep ruptured alloy 2.5Mo0.6W, with arrows indicating the direction of applied stress. (a) 850 °C/650 MPa, (b) 982 °C/248 MPa, (c) 1040 °C/145 MPa.